Simultaneous field enhancement and loss inhibition based on surface plasmon polariton mode hybridization

Xiaoyi Liu, Jinbo Gao, Yanchao Wang, Xiaoyi Wang, Haigui Yang, Haixiang Hu, Jinsong Gao, Tarik Bourouina, Tianhong Cui

To cite this version:

Xiaoyi Liu, Jinbo Gao, Yanchao Wang, Xiaoyi Wang, Haigui Yang, et al.. Simultaneous field enhancement and loss inhibition based on surface plasmon polariton mode hybridization. Nanophotonics, 2020, 10.1515/nanoph-2020-0023 . hal-02750156

HAL Id: hal-02750156
https://hal.science/hal-02750156

Submitted on 13 Jul 2020

Research article

Xiaoyi Liu, Jinbo Gao, Yanchao Wang, Xiaoyi Wang, Haigui Yang, Haixiang Hu, Jinsong Gao, Tarik Bourouina* and Tianhong Cui

Simultaneous field enhancement and loss inhibition based on surface plasmon polariton mode hybridization

https://doi.org/10.1515/nanoph-2020-0023
Received January 13, 2020; revised March 2, 2020; accepted March 20, 2020

Abstract: In common plasmonic configurations, energy loss and field enhancement are mutually restricted. In a vast majority of cases, high confinement goes together with high loss, which is a serious limitation for some applications. In an attempt of breaking this rule, which holds true for surface plasmon polariton (SPP) resonators, a multilayer trench grating microstructure with an asymmetric waveguide is considered. It supports both Fabry-Perot (FP) and cavity modes, whose hybridization exhibits unusual properties. The electric field enhancement was modulated by regulating the corresponding absorption and radiation quality factors. At the same time, energy loss was reduced, which is fundamentally ascribed to the mutual recycling of radiation energy between FP and cavity resonators. The maximum total quality factor and strongest field enhancement were both observed at the vicinity of quasi-static limit, thereby signifying that the structure exhibited simultaneous optimizations of field enhancement and loss inhibition, which is crucial to the design of high-quality SPP-based devices.

Keywords: nanophotonics; plasmonics; optical cavity; surface plasmon polariton; field enhancement; loss inhibition.

1 Introduction

In the area of high-quality plasmonic structure research, the reduction of energy loss without weakening the energy confinement is a crucial issue. On the one hand, the strong enhancement and the ultra-small mode volume of the electromagnetic field are among the main characteristics of some plasmonic structures, especially optical antennas [1–3], which bring into play a first class of potential applications to sensitive photodetection [4], surface-enhanced Raman spectroscopy [5, 6], nonlinear nanophotonics [7], infrared absorption enhancement [8–10], and display technologies [11, 12]. On the other hand, the configurations with low losses and high-quality factor (Q) values are strictly required in another class of applications to interferometer waveguides [13], ring resonators [14–16], and plasmon nanolasers [17–20]. However, it is difficult to simultaneously realize a significant field confinement together with a low loss based upon individual plasmonic structures [21], and that is why most designs have to be functionally oriented.

Recently, much attention has been devoted to engineering of composite structures to realize the trade-off between loss inhibition and field enhancement through coupling different plasmonic modes. Localized surface plasmon resonances (LSPRs) can couple with diffractive surface waves in nano disk arrays to obtain a relatively large Purcell factor, thereby implying the presence of both

---

***Corresponding author: Tarik Bourouina,** ESYCOM Lab, UMR 9007 CNRS, Univ Gustave Eiffel, 77454 Marne-la-Vallée, France, e-mail: tarik.bourouina@esiee.fr. https://orcid.org/0000-0003-2342-7149
Xiaoyi Liu: Key Laboratory of Optical System Advanced Manufacturing Technology, Changchun Institute of Optics, Fine Mechanics and Physics, Chinese Academy of Sciences, Changchun 130033, China; University of the Chinese Academy of Sciences, Beijing 100039, China; Fondation de l'Ecole normale supérieure, Paris 75005, France; and ESYCOM Lab, UMR 9007 CNRS, Univ Gustave Eiffel, 77454 Marne-la-Vallée, France
Jinbo Gao and Jinsong Gao: Key Laboratory of Optical System Advanced Manufacturing Technology, Changchun Institute of Optics, Fine Mechanics and Physics, Chinese Academy of Sciences, Changchun 130033, China; and University of the Chinese Academy of Sciences, Beijing 100039, China
Yanchao Wang, Xiaoyi Wang, Haigui Yang and Haixiang Hu: Key Laboratory of Optical System Advanced Manufacturing Technology, Changchun Institute of Optics, Fine Mechanics and Physics, Chinese Academy of Sciences, Changchun 130033, China
Tianhong Cui: Fondation de l'Ecole normale supérieure, Paris 75005, France; ESYCOM Lab, UMR 9007 CNRS, Univ Gustave Eiffel, 77454 Marne-la-Vallée, France; and Department of Mechanical Engineering, University of Minnesota, Minneapolis MN 55455, USA

a low loss and small mode volume [22]. The combination of the LSPRs with whispering gallery mode results in an extremely high *Q* factor within an optical microfiber [23]. Another line of thought to improve the structure's quality is to associate LSPRs with the photonic states [24]. On the contrary, relevant research on the hybridization of non-localized modes, namely, surface plasmon polaritons (SPPs), is rarely reported. SPP structures usually have advantages of tunability and resonance multiplexing over LSPRs [25]. More importantly, many SPP-based devices relying on waveguides are functionally irreplaceable [13]. SPP modes have also proven further control capabilities [26, 27], although the resulting better confinement or lower loss were obtained at the expense of increased structural complexity. Therefore, simpler and more practical schemes require further investigation as reported in this work.

The present study demonstrates a compound grating microstructure comprising multilayer stripes and trenches supporting two classes of SPP modes. Through SPP mode hybridization, the simultaneous optimization of field enhancement and loss inhibition can be achieved at the vicinity of quasi-static limit. Compared with all configurations involving LSPRs, this compound structure was much easier and more practical for precisely modulating the loss and field distribution through proper thickness control of a thin-film dielectric coating. A detailed discussion on the underlying mechanisms is given below.

2 Results and discussion

2.1 Illustrations of the designed multilayer trench gratings

The diagram of a unit cell of the compound periodic microstructure is presented in Figure 1A. The stripe waveguide was formed by two asymmetric metal-dielectric-dielectric (MDD) units. Silicon dioxide (SiO_2) and silicon (Si) were respectively categorized as the core and the cladding dielectric layers, and this configuration is capable of effectively binding the light. The SiO_2 layer thickness (*h*) is the key parameter in this study. The material of the metal layer is aluminum (Al). Different from the common metal-dielectric-metal (MDM) unit, such asymmetric MDD waveguide will effectively inhibit the absorption loss induced by compact metal layers, which will be proved by related calculations below and, eventually, through experimental validation. Figure 1B presents the cross-sectional scanning electron microscope (SEM) image, and the inset exhibits the detail of a fabricated MDD multilayer configuration. In this compound structure, Fabry-Perot (FP) resonances were excited laterally along the width of multilayer grating stripes and coupled with the cavity resonant modes excited within the adjacent trenches, thereby resulting in mode hybridization.

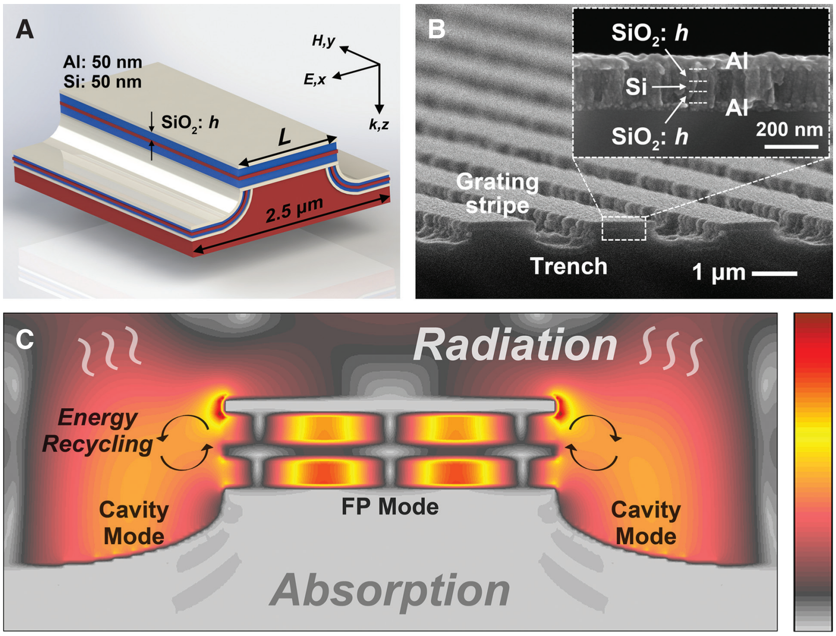

Figure 1: Schematic and physical illustrations of the designed multilayer trench gratings.
(A) Schematic diagram of a unit cell of the designed structure. (B) Cross-sectional SEM image of the microstructure, and the inset exhibits the detail of fabricated multilayer MDD configuration. (C) Working principle diagram of the designed structure. The normalized color bar ranges from 0 to 1 for gray and red, respectively.

The electric field enhancement was optimized by regulating the absorption and radiation quality factors in each mode configuration. Meanwhile, the effect of loss inhibition achieved by hybridization of two SPP modes in the compound structure was clearly presented based on a comparison of the various quality factors related to each part and the entire structure. The loss inhibition was fundamentally ascribed to the mutual recycling of radiation energy between the two adjacent modes. The maximization conditions of field enhancement and loss reduction were both generated at the quasi-static limit of the SiO_2 layer thickness. The working principle of this designed structure is simply exhibited in Figure 1C.

2.2 Electric field enhancement modulation

To illustrate the strong confinement in the MDD waveguide, the simulated electric field intensity distribution and the cross-sectional field plots along the dashed lines of the grating stripe part are presented in Figure 2A. The standing SPP in the multilayer waveguide formed a typical FP resonance mode in the horizontal direction (x direction) [28, 29]. The diffusion of energy was effectively obstructed by the Si layer with a high real part of permittivity in the longitudinal direction (z direction), thereby resulting in an extremely small mode volume [30, 31]. FP modes with the same resonance order exhibited a maximum electric field intensity in the vicinity of point A for all thicknesses. Figure 2B presents the dependence of the electric field enhancement on thickness. According to Seok et al., the interesting relationship between the field enhancement and the structure's quality factors can be defined as follows [32] (Supporting Information, Section 1):

$$\frac{|E_{\text{loc}}|^2_{\max}}{|E_{\text{i}}|^2}=\frac{2A_{\text{c}}\lambda_{\text{r}}Q^2_{\text{abs}}Q_{\text{rad}}}{\pi V_{\text{eff}}(Q_{\text{rad}}+Q_{\text{abs}})^2} \tag{1}$$

where λ_{r} is the resonance wavelength; $|E_{\text{loc}}|_{\max}$ and E_{i} are the maximum value of electric field intensity in the concerned area and the incident field amplitude, respectively; A_{c} is the effective aperture of the microstructure; V_{eff} is the effective mode volume of the concerned configuration, which is defined by the half-max electric field intensity in the designed structure (Supporting Information, Section 2); Q_{rad} and Q_{abs} are the radiation and absorption quality factors of the concerned structure, respectively. Clearly, the field enhancement is closely related to the values of Q_{rad} and Q_{abs}, thereby signifying that the maximum electric field enhancement of the designed configuration can be obtained by regulating its radiation and absorption characteristics. In addition, the total quality factor, Q_{tot}, of the configuration is the inverse summation of Q_{rad} and Q_{abs} such that $1/Q_{\text{tot}}=1/Q_{\text{rad}}+1/Q_{\text{abs}}$ [32]. Consequently, the values of Q_{rad} and Q_{abs} can be derived from Q_{tot} and Eq. (1). Firstly, in this FP waveguide, the total quality factor $Q^{\text{FP}}_{\text{tot}}$ is expressed as follows [33] (Supporting Information, Section 3):

$$Q^{\text{FP}}_{\text{tot}}=\frac{-\lambda_{\text{r}}L}{1-\exp(-\alpha L)}\frac{\partial\text{Re}(\beta)}{\partial\lambda} \tag{2}$$

where L is the length of FP waveguide, namely, the width of the grating stripe; β is the complex propagation constant of SPP; and α is the absorption coefficient with the relationship $\alpha=2\text{Im}(\beta)$ [33]. Obviously, the calculation of β is the key to calculating the value of $Q^{\text{FP}}_{\text{tot}}$. On the basis of the asymmetric MDD waveguide theory, the propagation constant β can be directly solved by the relevant dispersion equations related to the complex permittivity of each material (Supporting Information, Section 3), thereby successively calculating $Q^{\text{FP}}_{\text{tot}}$, $Q^{\text{FP}}_{\text{abs}}$, and $Q^{\text{FP}}_{\text{rad}}$. In simulations, we extracted the data of each material from literature [34, 35] and drew their fitting curves to conduct calculations; with regard to the calculations in experiments, the practical material data measured by ellipsometer were adopted. Consequently, the simulated and experimental results can be mutually validated to guarantee the correctness. Both the absorption Q values of such MDD configuration calculated by simulated and experimental data are much higher than that of conventional MDM unit [36], exhibiting an obvious inhibition effect of absorption loss due to the absence of compact metal layers (Supporting Information, Section 4). Notice that Eq. (2) should be modified when h is less than 20 nm (gray area in Figure 2B and C) because the Q factor of the designed waveguide configuration is only determined by the complex permittivity of the Al layer under the following quasi-static approximation [33, 37]:

$${}^{s}Q^{\text{FP}}_{\text{tot}}=\frac{\omega_{\text{r}}}{2\text{Im}(\varepsilon_{\text{Al}})}\frac{\partial\text{Re}(\varepsilon_{\text{Al}})}{\partial\omega} \tag{3}$$

where ε_{Al} is the complex permittivity of the Al layer, and ω_{r} is the resonance frequency. Following the above calculations, each Q factor of the grating stripe part will be precisely solved. Figure 2C presents the simulated and experimental dependences of the $Q^{\text{FP}}_{\text{rad}}$ and $Q^{\text{FP}}_{\text{abs}}$ on the SiO_2 layer thickness h. According to Eq. (1), if the field enhancement of the stripe part is considered as a function of $Q^{\text{FP}}_{\text{rad}}$,

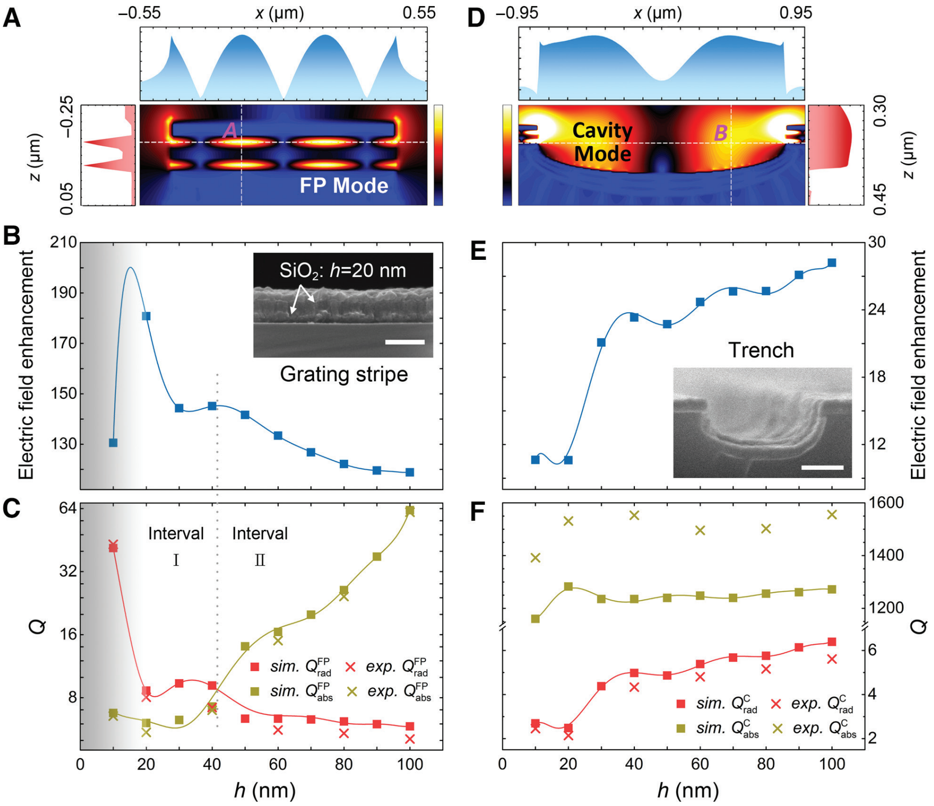

Figure 2: Relationships between electric field enhancement, absorption, and radiation characters in the designed structure. (A) Electric field intensity distribution and the cross-sectional field plots along the dashed lines of the grating stripe part supporting an FP mode. The color bar ranges from 0 to 13 for blue and white, respectively. (B) Dependence of the electric field enhancement of the grating stripe part on h. The inset is the SEM image of the multilayer grating stripe part with $h = 20$ nm. The scale bar is 200 nm. (C) Dependences of Q^{FP}_{rad} and Q^{FP}_{abs} on h. The symbols "■" and "×" respectively represent the simulated and experimental results. The gray areas in (B) and (C) represent the applicable region of quasi-static approximation. (D) Electric field intensity distribution and the cross-sectional field plots along the dashed lines of the trench part supporting a cavity (C) mode. The color bar ranges from 0 to 4. (E) Dependence of the electric field enhancement of the trench part on h. The inset is the SEM image of the trench part, and the scale bar is 500 nm. (F) Dependences of Q^{C}_{rad} and Q^{C}_{abs} on h. The symbols "■" and "×" respectively represent the simulated and experimental results. The solid curves are polynomial fit of simulated data points.

the maximization condition can be clarified by taking a derivative with respect to Q^{FP}_{rad} (Supporting Information, Section 1). Seok et al. defined the maximization condition $Q_{rad} = Q_{abs}$ because it makes the derivative become 0 [32]. Notice that there is an implied specific condition in their research that for the dielectric layer thickness, their Q_{rad} is almost a monotonic function in the waveband of interest. Therefore, for the maximum of field enhancement, the zero point of derivative is the unique solution. Recently, Liu et al. demonstrated a beautiful work that an extreme high field enhancement was realized through the combination of localized plasmonic nanoantennas and a photonic crystal microcavity with the identical optimum condition, and the tendency change of Q_{rad} was still not considered [38]. However, in the present study, the value of Q^{FP}_{rad} is not monotonic anymore for the selected values of SiO$_2$ layer thickness h. If merely considering the condition $Q_{rad} = Q_{abs}$, only the local optimum would be obtained instead of the global one. In this case, the inflection points of Q^{FP}_{rad} must be considered as well. Figure 2B and C indicate that the field enhancement and Q^{FP}_{rad} have the same monotonicity when $Q_{abs} > Q_{rad}$ (Interval II) and are opposite when $Q_{abs} < Q_{rad}$ (Interval I), which accords well with the variation trend predicted by Eq. (S3). Obviously, the maximum field enhancement was observed in the vicinity of 20-nm thickness, which is attributed to the sudden change of the monotonicity of Q^{FP}_{rad} near the quasi-static limit. It provides an original approach to enhance the electric field in the plasmonic waveguide, namely, to engineer the structure's radiation and absorption characteristics so as to achieve the maximization condition, especially by virtue of the quasi-static limit. Meanwhile, the effective mode volume V_{eff} in the grating stripe part gradually shrunk when decreasing h from large volume towards the vicinity of quasi-static limit (Supporting Information, Figure S1), signifying that the optimization of V_{eff} can also be achieved accompanied by the maximization of electric field enhancement. It is worth noting that quasi-static approximation is a concept of dimension which is merely applicable to tiny structures far less than incident wavelength [33]. It means the quasi-static limit position can only be defined within an approximate range rather than by a precise value. To further approach the precise thickness of maximum field enhancement, numerical simulations with high accuracy have to be taken into account.

Similarly, Figure 2D presents the simulated electric field intensity distribution of the cavity resonance mode (C) in the trench, and Figure 2E displays the dependence of the field enhancement on *h*. The maximum electric field intensity was extracted in the vicinity of point B. As compared to the FP resonance mode, the corresponding absorption quality factor $Q_{\mathrm{abs}}^{\mathrm{C}}$ in the trench part was first derived based on the following equation [39]:

$$Q_{\mathrm{abs}}^{\mathrm{C}} = \frac{\pi}{\lambda_{\mathrm{r}}\,\mathrm{Im}(\beta)} \tag{4}$$

where β is the complex propagation constant of the cavity resonance mode, which can be solved by the dispersion equation at the single interface [39] (Supporting Information, Section 3). Subsequently, its total and radiation *Q* values were solved simultaneously. Figure 2F presents the simulated and experimental dependences of $Q_{\mathrm{rad}}^{\mathrm{C}}$ and $Q_{\mathrm{abs}}^{\mathrm{C}}$ on the $\mathrm{SiO_2}$ layer thickness *h*. The results satisfy the general rule of the semi-open architecture structure wherein its radiation loss cannot be ignored [40]. When radiation occupies the dominance of loss, $Q_{\mathrm{abs}}^{\mathrm{C}}$ will become extremely large. For simulated and experimental results, any minor difference in $Q_{\mathrm{rad}}^{\mathrm{C}}$ or $Q_{\mathrm{tot}}^{\mathrm{C}}$ will generate a significant discrepancy between simulated and tested values of $Q_{\mathrm{abs}}^{\mathrm{C}}$, as shown in Figure 2F. Because the values of $Q_{\mathrm{abs}}^{\mathrm{C}}$ are always larger than the values of $Q_{\mathrm{rad}}^{\mathrm{C}}$, according to Eq. (S3), the field enhancement and $Q_{\mathrm{rad}}^{\mathrm{C}}$ must maintain the same monotonicity in the concerned waveband, and every inflection point of $Q_{\mathrm{rad}}^{\mathrm{C}}$ must correspond to a local extreme point of the field enhancement. As expected, this phenomenon can be clearly observed in Figure 2E and F.

2.3 Loss inhibition based on energy mutual recycling

After discussing the quality factors of the grating stripe and trench, respectively, the loss characteristics of the entire configuration were investigated by the coupled mode theory [32, 41]. Directly, the total *Q* factors of the multilayer trench grating structure were extracted as $Q_{\mathrm{tot}} = \lambda_r/\Delta\lambda$ by fitting a Lorentzian curve to the measured reflectance spectrum (*R*) [22, 32], as exhibited in Figure 3A, where $\Delta\lambda$ is the full width at the half maximum of the resonance peak. The total radiation *Q* factors were then calculated as follows [32, 41] (Supporting Information, Section 5):

$$Q_{\mathrm{rad}}^{\mathrm{tot}} = \frac{2Q_{\mathrm{tot}}}{1+\sqrt{2R(\omega_{\mathrm{r}})-1}} \tag{5}$$

Following above calculations, the total absorption *Q* factors were also obtained by the relationship $1/\mathrm{Q}_{\mathrm{abs}}^{\mathrm{tot}} = 1/Q_{\mathrm{tot}} - 1/\mathrm{Q}_{\mathrm{rod}}^{\mathrm{tot}}$. Figure 3B exhibits the comparison between the multiple absorption *Q* factors, including $Q_{\mathrm{abs}}^{\mathrm{FP}}$, $Q_{\mathrm{abs}}^{\mathrm{C}}$, and $Q_{\mathrm{abs}}^{\mathrm{tot}}$, as well as the radiation *Q* factors. Interestingly enough, the majority of $Q_{\mathrm{abs}}^{\mathrm{tot}}$ values are in between $Q_{\mathrm{abs}}^{\mathrm{FP}}$ and $Q_{\mathrm{abs}}^{\mathrm{C}}$, but the majority of $Q_{\mathrm{rad}}^{\mathrm{tot}}$ values are larger than the values of both $Q_{\mathrm{rad}}^{\mathrm{FP}}$ and $Q_{\mathrm{rad}}^{\mathrm{C}}$. The latter results indicate that with respect to the characteristic of radiation loss inhibition, the hybrid mode was better than both FP and cavity modes taken individually. Intuitively, this is obviously an unusual situation that the radiation of the entire structure is less than that part of that structure. Therefore, understanding the underlying mechanism requires further examination.

To explain this unusual observed phenomenon, the Poynting vector diagram of the compound configuration, reflecting the strong flow and transmission of the energies between the grating stripe and the trench parts, is presented in Figure 4A. Obviously, when calculating the radiation losses of the individual grating stripe and trench structures, the energy exchange in the modes hybridization process was not taken into account. In fact, the real escaped energy was a small proportion of the radiation, while the major portion was mutually reclaimed by the FP and cavity modes. The essence of the loss inhibition for mode hybridization may be defined by the energy mutual recycling between the two SPP modes, resulting in a reduction in the radiation loss of the entire microstructure, thereby reducing the total loss. As expected, the total loss of the compound configuration was always less than both the values of the two individual parts within all the selected values of $\mathrm{SiO_2}$ layer thickness, as highlighted in Figure 4B. Wang et al. once had a worry that the radiation loss would grow rapidly following an increase in the nanostructure size, and it was then unclear whether the *Q* factor would increase beyond the quasi-static limit. For larger *Q* values, strong radiation should be forbidden [37]. The designed compound structure offered in the present study provided a solution in which, although the radiation loss of the grating stripe grew dramatically within the

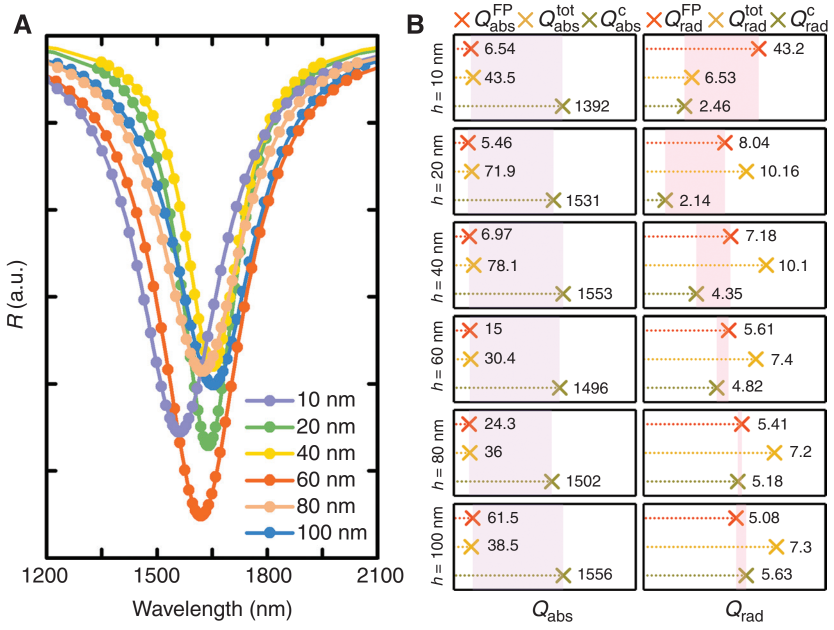

Figure 3: Comparisons of absorption and radiation characters between FP mode, cavity mode, and the total structure, respectively. (A) Measured reflectance curves with different *h* values treated by the Lorentzian fitting. (B) Left column: comparison between the experimental values of Q_{abs}^{FP}, Q_{abs}^{C}, and Q_{abs}^{tot} at different *h* values. Right column: comparison between the experimental values of Q_{rad}^{FP}, Q_{rad}^{C}, and Q_{rad}^{tot} at different *h* values. Majority of Q_{abs}^{tot} values are in between Q_{abs}^{FP} and Q_{abs}^{C} (in the colorful area), whereas the majority of Q_{rad}^{tot} values are larger than both Q_{rad}^{FP} and Q_{rad}^{C} (beyond the colorful area).

quasi-static limit (see Figure 2C, from 10 nm to 20 nm), it exhibited a decrease in the total loss of the entire configuration due to the mode hybridization. The Q_{tot} reached a relatively high point when *h* was about 20 nm (boundary of the gray area in Figure 4B corresponding to the quasi-static limit). Moreover, the maximum field enhancement in the grating stripe was also observed under this condition (see Figure 4B), thereby exhibiting a nice combination of loss inhibition and field convergence. Although the above significant effects are obtained at the expense of additional effective mode volume of cavity mode, the proposed approach for improving the performance of widely used SPP-based composite structures is indeed effective, which is fundamentally distinguished from the LSPR-based work of Seok et al., and therefore worth taking this step forward.

3 Conclusions

In summary, a multilayer trench grating microstructure comprising grating stripe and trench parts was demonstrated. The former configuration was capable of exciting the FP resonance mode in the MDD grating stripe waveguide with a relatively low absorption loss compared with the mode excited in common MDM configuration, while the latter formed the cavity resonance mode adjacent to the FP mode. In each configuration, maximum electric field enhancement was achieved by regulating the corresponding absorption and radiation *Q* factors. Especially, the maximization of electric field enhancement in grating stripe part was achieved at the quasi-static limit accompanied by a tiny effective mode volume of FP mode. Meanwhile, loss reduction in SPP-mode hybridization was observed through the comparison between the quality factors belonging to each part and to the entire structure. The energy mutual recycling between FP modes and cavity modes resulted in a reduced radiation loss for the entire microstructure, which may be the essence of loss inhibition through hybridization of the two SPP modes. In addition, the total quality factor also achieved the optimum at the vicinity of quasi-static limit, thereby signifying a nice combination between the field enhancement and energy loss inhibition.

4 Methods

4.1 Fabrication of multilayer trench gratings

The designed structure was fabricated by laser direct writing (LDW) lithography (Heidelberg, Germany, DWL

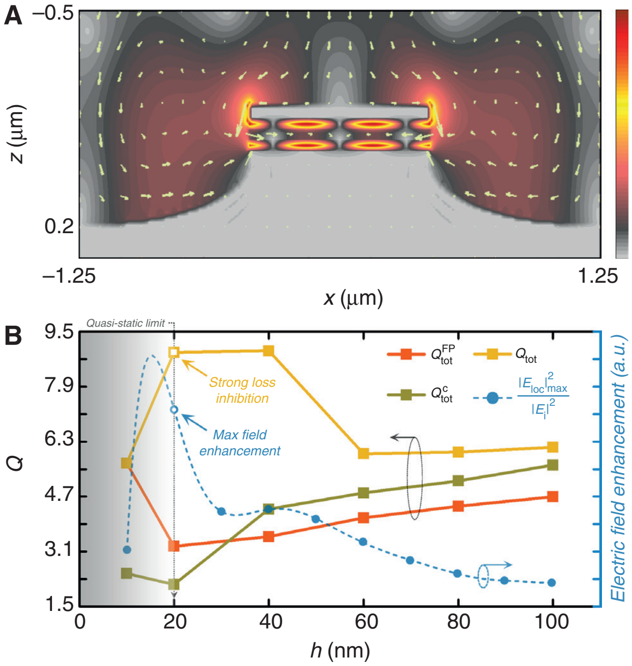

Figure 4: Loss inhibition is ascribed to the energy recycling between FP and cavity modes.
(A) Poynting vector diagram of the multilayer trench grating structure with $h = 20$ nm. The background is the electric field intensity distribution of designed microstructure, and the color bar ranges from 0 to 14. (B) Dependences of the experimental values of Q_{tot}^{FP}, Q_{tot}^{C}, and Q_{tot} on h. The dependence of the electric field enhancement of the grating stripe part on h is also given as reference. The gray area represents the applicable region of the quasi-static approximation.

4000). The photoresist was first deposited on polished clean Si wafers by spin coating with a thickness of about 450 nm. The samples were then patterned by the LDW method and subsequently developed for 40 s in sodium hydroxide (NaOH) solution. The samples were etched by reactive ion etching in an SF_6 plasma for 40 s so as to obtain the 400-nm-deep trenches with a grating constant of 2.5 μm. Following soaking in the acetone solution to clear the residual photoresist, the samples were then processed in a magnetron sputtering reactor to realize the film coating process, thereby resulting in five alternate layers: Al, SiO_2, Si, SiO_2, and Al. The layer thicknesses of Si and Al were both 50 nm, while the SiO_2 layers had different thicknesses, including 10 nm, 20 nm, 40 nm, 60 nm, 80 nm, and 100 nm. The complex permittivity of each material involved in experimental calculations were measured by ellipsometer. In order to enable excitation of the hybrid mode or the simultaneous excitations of the FP and cavity resonances, the width ratios between the grating stripe and trench were approximately set from 0.67 to 0.79, which were derived from previous simulations.

4.2 Reflectance spectral response measurement

The integrated reflectance spectral responses of the fabricated samples were measured using a spectrometer equipped with a 160-mm integrating sphere in the wavelength range from 500 nm to 2500 nm for the sake of calculating the Q factors of the configurations as well as other relevant parameters. The resolution of the spectrometer is 4 nm, and the normal incidence light in the spectrometer is unpolarized.

4.3 Modeling and simulations

The designed structure was theoretically analyzed through the finite difference-time domain method. In both x and y directions, the periodic condition was adopted as the boundary condition, and the perfectly matched layer condition was used in the z direction. A plane wave with linear polarization perpendicular to the gratings was adopted as the normal incidence source. Through simulations, it can be proved that the calculation results of electric field enhancement and various quality factors will remain the same when changing the incidence to an unpolarized one. The mesh accuracy in models is 10 nm. The material characteristic parameters of Si and SiO_2 such as the permittivity and refractive index were extracted from the database of Palik [34], and the Al parameters were extracted from Shiles et al. [35]. The width ratio of the two parts of the unit cell were optimized by simulations to support the formation of the hybrid mode, where an FP mode is strongly coupled to a cavity mode. The SiO_2 layer thickness was also varied from 10 nm to 100 nm in a series of simulations to carefully examine the relationship between the field enhancement and the quality factors.

Supporting Information accompanies this paper at https://doi.org/10.1515/nanoph-2020-0023.

Acknowledgments: This project was supported by the National Natural Science Foundation of China (Nos. 61675199, Funder Id: http://dx.doi.org/10.13039/501100001809 and U1435210). The authors would like to thank Dr. Chengli Guo, Dr. Haisong Wei, Dr. Xiaolin Yin, and Dr. Ke Wang at Key Laboratory of Optical System Advanced Manufacturing Technology, Changchun Institute of Optics, Fine Mechanics and Physics, Chinese Academy of Sciences for technical assistance. Funder Name: Agence Nationale de la Recherche, Funder Id: http://dx.doi.org/10.13039/501100001665, Grant Number: ANR-16-IDEX-0003. Funder Name: Fondation ENS, Grant Number: Chaire Blaise Pascal.

Competing financial interests: The authors declare no competing financial interests.

References

[1] Knight MW, Sobhani H, Nordlander P, Halas NJ. Photodetection with active optical antennas. Science 2011;332:702–4.
[2] Rodriguez SRK, Abass A, Maes B, Janssen OTA, Vecchi G, Rivas JG. Coupling bright and dark plasmonic lattice resonances. Phys Rev X 2011;1:021019.
[3] Lin KT, Chen HL, Lai YS, Yu CC. Silicon-based broadband antenna for high responsivity and polarization-insensitive photodetection at telecommunication wavelengths. Nat Commun 2014;5:3288.
[4] Tang L, Kocabas SE, Salman L, et al. Nanometre-scale germanium photodetector enhanced by a near-infrared dipole antenna. Nat Photonics 2008;2:226–9.
[5] Nie S, Emory SR. Probing single molecules and single nanoparticles by surface-enhanced Raman scattering. Science 1997;275:1102–6.
[6] Kneipp K, Wang Y, Kneipp H, et al. Single molecule detection using surface-enhanced Raman scattering (SERS). Phys Rev Lett 1997;78:1667.
[7] Kauranen M, Zayats AV. Nonlinear plasmonics. Nat. Photonics 2012;6:737–48.
[8] Neubrech F, Huck C, Weber K, Pucci A, Giessen H. Surface-enhanced infrared spectroscopy using resonant nanoantennas. Chem Rev 2017;117:5110–45.
[9] Li W, Valentine J. Metamaterial perfect absorber based hot electron photodetection. Nano Lett 2014;14:3510–4.
[10] Brown LV, Yang X, Zhao K, Zheng BY, Nordlander P, Halas NJ. Fan-shaped gold nanoantennas above reflective substrates for surface-enhanced infrared absorption (SEIRA). Nano Lett 2015;15:1272–80.
[11] Kasperczyk M, Person S, Ananias D, Carlos LD, Novotny L. Excitation of magnetic dipole transitions at optical frequencies. Phys Rev Lett 2015;114:163903.
[12] Decker M, Staude I, Shishkin II, et al. Dual-channel spontaneous emission of quantum dots in magnetic metamaterials. Nat Commun 2013;4:2949.
[13] Bozhevolnyi SI, Volkov VS, Devaux E, Laluet JY, Ebbesen TW. Channel plasmon subwavelength waveguide components including interferometers and ring resonators. Nature 2006;440:508–11.
[14] Wang Z, Xu XC, Fan DL, Wang YG, Chen RT. High quality factor subwavelength grating waveguide micro-ring resonator based on trapezoidal silicon pillars. Opt Lett 2016;41:3375–8.
[15] Bogaerts W, DeHeyn P, Vaerenbergh TV, et al. Silicon microring resonators. Laser Photonics Rev 2012;6:47–73.
[16] Fang YF, Li SL, Mei YF. Modulation of high quality factors in rolled-up microcavities. Phys Rev A 2016;94:033804.
[17] Lu YJ, Wang CY, Kim J, et al. All-color plasmonic nanolasers with ultralow thresholds: autotuning mechanism for single-mode lasing. Nano Lett 2014;14:4381–8.
[18] Noginov MA, Zhu G, Belgrave AM, et al. Demonstration of a spaser-based nanolaser. Nature 2009;460:1110–2.
[19] Li DB, Stockman MI. Electric spaser in the extreme quantum limit. Phys Rev Lett 2013;110:106803.
[20] Ding K, Ning CZ. Metallic subwavelength-cavity semiconductor nanolasers. Light Sci Appl 2012;1:e20.
[21] Wang JF, Zhang C, Zhang JH, et al. Hybrid plasmonic cavity modes in arrays of gold nanotubes. Adv Opt Mater 2017;5:1600731.
[22] Todisco F, Esposito M, Panaro S, et al. Toward cavity quantum electrodynamics with hybrid photon gap-plasmon states. ACS Nano 2016;10:11360–8.
[23] Wang P, Wang YP, Yang ZY, et al. Single-band 2-nm-line-width plasmon resonance in a strongly coupled Au nanorod. Nano Lett 2015;15:7581–6.
[24] Vecchi G, Giannini V, Rivas JG. Shaping the fluorescent emission by lattice resonances in plasmonic crystals of nanoantennas. Phys Rev Lett 2009;102:146807.
[25] Liu XY, Gao JS, Yang HG, Wang XY, Guo CL. Multiple infrared bands absorber based on multilayer gratings. Opt Commun 2018;410:438–42.
[26] Bozhevolnyi SI, Volkov VS, Devaux E, Ebbesen TW. Channel plasmon-polariton guiding by subwavelength metal grooves. Phys Rev Lett 2005;95:046802.
[27] Haffner C, Chelladurai D, Fedoryshyn Y, et al. Low-loss plasmon-assisted electro-optic modulator. Nature 2018;556:483–6.
[28] Bora M, Behymer EM, Dehlinger DA, et al. Plasmonic black metals in resonant nanocavities. Appl Phys Lett 2013;102:251105.
[29] Hu FF, Yi HX, Zhou ZP. Band-pass plasmonic slot filter with band selection and spectrally splitting capabilities. Opt Express 2011;19:4848–55.
[30] Oulton RF, Sorger VJ, Zentgraf T, et al. Plasmon lasers at deep subwavelength scale. Nature 2009;461:629–32.
[31] Oulton RF, Sorger VJ, Genov DA, Pile DFP, Zhang X. A hybrid plasmonic waveguide for subwavelength confinement and long-range propagation. Nat Photonics 2008;2:496–500.
[32] Seok TJ, Jamshidi A, Kim M, et al. Radiation engineering of optical antennas for maximum field enhancement. Nano Lett 2011;11:2606–10.
[33] Yang J, Sauvan C, Jouanin A, Collin S, Pelouard JL, Lalanne P. Ultrasmall metal-insulator-metal nanoresonators: impact of slow-wave effects on the quality factor. Opt Express 2012;20:16880–91.
[34] Palik E. Handbook of optical constants of solids. Cambridge, MA, USA, Academic Press, 1998.
[35] Shiles E, Sasaki T, Inokuti M, Smith DY. Self-consistency and sum-rule tests in the Kramers-Kronig analysis of optical data: applications to aluminum. Phys Rev B 1980;22:1612–28.
[36] Liu XY, Gao JB, Gao JS, et al. Microcavity electrodynamics of hybrid surface plasmon polariton modes in high-quality multilayer trench gratings. Light Sci Appl 2018;7:14.
[37] Wang F, Shen YR. General properties of local plasmons in metal nanostructures. Phys Rev Lett 2006;97:206806.
[38] Liu JN, Huang QL, Liu KK, Singamaneni S, Cunningham BT. Nanoantenna-microcavity hybrids with highly cooperative plasmonic-photonic coupling. Nano Lett 2017;17:7569–77.
[39] Liu XY, Gao JS, Yang HG, Wang XY, Tian SC, Guo CL. Hybrid plasmonic modes in multilayer trench grating structures. Adv Opt Mater 2017;5:1700496.
[40] Bozhevolnyi SI, Søndergaard T. General properties of slow-plasmon resonant nanostructures: nano-antennas and resonators. Opt Express 2007;15:10869–77.
[41] Hamam RE, Karalis A, Joannopoulos JD, Soljačić M. Coupled-mode theory for general free-space resonant scattering of waves. Phys Rev A 2007;75:053801.

Supplementary Material: The online version of this article offers supplementary material (https://doi.org/10.1515/nanoph-2020-0023).